Neurochemical Research (2020) 45:53–67
https://doi.org/10.1007/s11064-019-02819-z

ORIGINAL PAPER

Integrity of White Matter is Compromised in Mice with Hyaluronan Deficiency

Ang D. Sherpa[1,9] · David N. Guilfoyle[2] · Aditi A. Naik[1,3,4,5] · Jasmina Isakovic[1,10] · Fumitoshi Irie[6] · Yu Yamaguchi[6] · Jan Hrabe[2,5] · Chiye Aoki[1,7] · Sabina Hrabetova[5,8]

Received: 9 April 2019 / Revised: 16 May 2019 / Accepted: 22 May 2019 / Published online: 7 June 2019

Abstract

Brain white matter is the means of efficient signal propagation in brain and its dysfunction is associated with many neurological disorders. We studied the effect of hyaluronan deficiency on the integrity of myelin in murine corpus callosum. Conditional knockout mice lacking the hyaluronan synthase 2 were compared with control mice. Ultrastructural analysis by electron microscopy revealed a higher proportion of myelin lamellae intruding into axons of knockout mice, along with significantly slimmer axons (excluding myelin sheath thickness), lower g-ratios, and frequent loosening of the myelin wrappings, even though the myelin thickness was similar across the genotypes. Analysis of extracellular diffusion of a small marker molecule tetramethylammonium (74 MW) in brain slices prepared from corpus callosum showed that the extracellular space volume increased significantly in the knockout animals. Despite this vastly enlarged volume, extracellular diffusion rates were significantly reduced, indicating that the compromised myelin wrappings expose more complex geometric structure than the healthy ones. This finding was confirmed in vivo by diffusion-weighted magnetic resonance imaging. Magnetic resonance spectroscopy suggested that water was released from within the myelin sheaths. Our results indicate that hyaluronan is essential for the correct formation of tight myelin wrappings around the axons in white matter.

Keywords Hyaluronan · Myelin · Axon · Diffusion · Electron microscopy · Magnetic resonance

Special Issue: In honor of Prof Eva Sykova.

✉ Jan Hrabe
jan.hrabe@nki.rfmh.org

✉ Chiye Aoki
ca3@nyu.edu

✉ Sabina Hrabetova
sabina.hrabetova@downstate.edu

[1] Center for Neural Science, New York University, 4 Washington Place, New York, NY 10003, USA

[2] Medical Physics Laboratory, Center for Biomedical Imaging and Neuromodulation, Nathan S. Kline Institute, 140 Old Orangeburg Road, Orangeburg, NY 10962, USA

[3] Department of Biology, New York University, 100 Washington Square East, 1009 Silver Center, New York, NY 10003, USA

[4] Neural and Behavioral Science Graduate Program, State University of New York Downstate Medical Center, 450 Clarkson Avenue, Brooklyn, NY 11203, USA

[5] Department of Cell Biology, State University of New York Downstate Medical Center, 450 Clarkson Avenue, Brooklyn, NY 11203, USA

[6] Human Genetics Program, Sanford Burnham Prebys Medical Discovery Institute, 10901 North Torrey Pines Road, La Jolla, CA 92037, USA

[7] Neuroscience Institute, New York University Langone Medical Center, 550 First Avenue, New York, NY 10016, USA

[8] The Robert F. Furchgott Center for Neural and Behavioral Science, State University of New York Downstate Medical Center, 450 Clarkson Avenue, Brooklyn, NY 11203, USA

[9] Present Address: Department of Neurosurgery, New York University School of Medicine, 550 First Avenue, New York, NY 10016, USA

[10] Present Address: Omnion Research International, Ul. Mirka Deanovića 9, 10000 Zagreb, Croatia

Introduction

Myelinated axons in the white matter of the nervous system allow rapid propagation of nerve impulses through neuronal networks. Changes in the white matter detected with diffusion tensor imaging have been correlated with higher order motor skills in humans such as piano playing [1] and juggling [2], while dysfunction in white matter is documented in brain disorders such as multiple sclerosis [3], cerebral palsy [4], traumatic brain injury [5] as well as mental illnesses and cognitive deficits [6, 7]. Recent work has implicated extracellular matrix (ECM) in white matter functionality. For example, Bekku and co-workers [8] found that a hyaluronan-binding link protein Bral1 is crucial for stabilizing the ECM assembly at the nodes of Ranvier and maintaining the integrity of nerve impulse propagation in corpus callosum (CC). Yet, there are few studies looking at ECM affecting the integrity of white matter.

ECM is a meshwork of glycosaminoglycans, proteoglycans and glycoproteins. Its components are interconnected to assemble a complex matrix that is involved in many biological processes including development, growth factor signaling, cell proliferation, migration, plasticity and homeostasis [9–11]. A major component of the ECM is a large polyanionic glycosaminoglycan hyaluronan (HA) with a molecular mass of 10^6–10^7 Da and an extended length of 2–25 µm [12]. HA has high binding capacity for water and occupies a very large molecular domain in solutions [12, 13]. It has previously been detected in central nervous system white matter [8, 14, 15] and one study suggested that it was present inside the myelin sheaths [16]. However, its role in the white matter remains largely unknown.

HA is synthesized by hyaluronan synthases. There are three hyaluronan synthase subtypes (HAS1, HAS2, and HAS3) in mammals. These HAS proteins reside in the plasma membranes and extrude nascent HA chains directly into the extracellular space [12]. Among the *Has* genes, *Has2* is highly expressed in white matter and conditional knockout of *Has2* in all three major neural cell types (*Nestin-Cre;Has2*$^{flox/flox}$, designated as *Has2*^{CKO} hereafter) results in a significant loss of HA along the major fiber tracts, such as the CC and the cingulum bundle [17]. *Has2*^{CKO} mice thus offer a suitable model for examining the impact of HA deficiency on white matter structural integrity and function.

Extracellular space (ECS) of the brain is a narrow space surrounding brain cells where diffusion-mediated transport of ions, molecules, and drug agents occurs [18]. ECM molecules are important for the preservation of physiologically optimal values of ECS parameters [8, 17, 19] which influence molecular transport through the ECS, namely the extracellular volume fraction and diffusion permeability [20, 21]. ECS volume fraction is defined as the ECS volume with respect to brain tissue volume, $\alpha = V_{ECS}/V_{tissue}$. Diffusion permeability is the effective diffusion coefficient D^* with respect to the diffusion coefficient in free solution, $\theta = D^*/D_{free}$. It quantifies how much the diffusion slows down in ECS relative to an obstacle free medium [21]. Alternatively, tortuosity defined as $1/\sqrt{\theta}$ could be used [22]. These parameters can be quantified with Real-Time Iontophoretic (RTI) method that employs tetramethylammonium (TMA) as an extracellular probe [22, 23]. The RTI method has been previously applied to regions containing prominent ensembles of oriented fibers where extracellular diffusion is anisotropic [24, 25]. Using the RTI method in the CC, Bekku et al. [8] found that D^* measured along and across fibers in CC increased in Bral1-deficient mice while α did not change.

In this study, we argue that the loss of HA disrupts myelin integrity and leads to alteration in ECS structure and to functional deficits. In order to test this hypothesis, we applied a multi-scale approach encompassing electron microscopy, diffusion analysis, and in vivo magnetic resonance imaging and spectroscopy in CC of control and *Has2*^{CKO} mice. In *Has2*^{CKO} mice, we found abnormalities in myelin sheaths and reduced axonal diameter at the ultrastructural level, grossly enlarged but less permeable ECS at the microscopic level, and reduced diffusional anisotropy at the macroscopic level in vivo.

Materials and Methods

Has2^{CKO} (*Nestin-Cre;Has2*$^{flox/flox}$) and *Has2*$^{flox/flox}$ mice were bred at Sanford Burnham Prebys Medical Discovery Institute as described previously [17] and C57BL6 mice were purchased from a commercial vendor. *Has2*$^{flox/flox}$ mice and C57BL6 mice served as control animals in this study. Data from *Has2*$^{flox/flox}$ mice and C57BL6 mice were pooled since we did not detect any differences in the results from these animals.

Brain Tissue Preparation for Electron Microscopy

For electron microscopy (EM) experiments, three control mice (C57BL6 or *Has2*$^{flox/flox}$; 6.5–8 months old, all female) and three *Has2*^{CKO} mice (6.5–8 months old, all female) were deeply anesthetized using standard protocol [26]. Anesthetized animals were then transcardially perfused with phosphate-buffered saline (0.01 M phosphate buffer in 0.9% sodium chloride, pH 7.4, containing heparin 10,000 U/ml, cat# 00069-0062-01; Pfizer Injectables, New York, NY, USA) followed by an aldehyde solution

(4% paraformaldehyde and 0.1% glutaraldehyde in 0.1 M phosphate buffer, pH 7.4) at a flow rate of 25 ml/min for 10 min. Brains were extracted and post-fixed in the aldehyde perfusate. Coronal sections of 50 µm thickness, containing CC, were prepared with a vibrating microtome (Leica VT 1000 S; Leica Microsystems, Wetzlar, Germany). Sections were post-fixed in 2% glutaraldehyde for 11 min and in 1.5% potassium ferrocyanide and 1% osmium tetroxide for an hour to preserve myelin ultrastructure [27]. The sections were dehydrated sequentially with 30%, 50% and 70% ethanol, and post-fixed overnight in 1% uranyl acetate in 70% ethanol solution at 4 °C. The next day, sections were post-fixed in 1% uranyl acetate in 70% ethanol again and further dehydrated in 90% and in 100% ethanol.

Following dehydration, sections were rinsed in 100% acetone, infiltrated with a mixture consisting of 50% acetone and 50% EPON-812, followed by 100% EPON-812 overnight at room temperature. Sections were flat embedded between two sheets of Aclar and cured in an oven at 60 °C for about 36 h. The flat embedded sections were capsule-embedded and cured at 60 °C for 40 h. Seventy-five nm thick ultra-thin sections parallel to the surfaces of coronal sections from the capsule embeds were prepared and collected on formvar-coated, 400 mesh thin-bar nickel grids. Ultra-thin sections were counterstained with lead citrate. Glutaraldehyde, osmium tetroxide, paraformaldehyde, EPON-812, uranyl acetate, lead citrate and grids were purchased from Electron Microscopy Sciences (Hatfield, PA, USA).

Electron Microscopy

Ultra-thin sections containing CC were viewed under an electron microscope (JOEL 1200EX II; JOEL Ltd, Tokyo, Japan) and images were captured with a CCD camera (AMT XR80; Advanced Microscopy Techniques, Woburn, MA, USA). The experimenter was blind to the identity of the genotype group during acquisition and analyses of the electron microscopic images. Twenty micrographs were analyzed from control brains and 20 micrographs were analyzed from $Has2^{CKO}$ brains. The micrographs from both groups were imaged at a magnification of 7500×. Each micrograph spanned an area of 468.78 μm^2 at a magnification of 7500×. Additional images at higher magnifications (20,000×, 30,000×, and 40,000×) were also obtained to record ultrastructural details. In summary, a total of 252 axons were analyzed from 3 control brains (a minimum of 49 axons from each animal) while a total of 197 axons were analyzed from 3 $Has2^{CKO}$ brains (a minimum of 60 axons from each animal). At most, 15 axonal profiles from ultra-thin sections were quantitatively analyzed from each micrograph.

Abnormalities of myelinated axons at the ultrastructural level such as intrusions, protrusions, waves, and separations per 1 µm of axon length of an axon were assessed. A myelin sheath intruding into an axon, making a semicircular loop, was categorized as an "intrusion" while a myelin sheath protruding outwardly along the length of an axon was categorized as a "protrusion". The presence of many such intrusions and protrusions following one another along the length of an axon was categorized as a "wave". A separation within the myelin sheaths or between the myelin sheath and the axonal membrane was categorized as a "separation" (Fig. 1). The area occupied by the separation was termed the "myelin separation area".

Tools of ImageJ version 1.50g (https://imagej.nih.gov/ij) were used to measure areas and lengths of axonal profiles and myelin sheaths. Axonal diameter was measured by drawing a line of minimum length, oriented perpendicularly to the longitudinal axis, running through the center of the axon to the inner limits of the myelin sheath. The myelinated axon diameter was measured by extending this line to the outer limits of myelin sheath. Myelin thickness was quantified by subtracting the axonal diameter from the myelinated axon diameter and dividing the result by 2. The g-ratio of a myelinated axon was calculated using an established approach, which estimates the ratio of axonal diameter to myelinated fiber diameter [28]. For assessing g-ratios, the axonal and the myelinated fiber diameters of axon profiles were selected based on the following criteria: (1) the two diameters were measured at the same point along the axonal length (2) the selected point along the axonal length represented a sector of the axon that appeared neither narrow nor wide but estimated, by eye, to represent roughly an average (3) the two diameters were not measured at a point along the axonal length where abnormalities were detected, such as intrusions, protrusions, waves, and separations (these abnormalities are described more in detail above) (4) if there were more than one point along the axonal length representative of the average diameter, then the smaller of the two diameters was selected, and (5) if the average diameter could not be identified because of continuous widening and/or narrowing of the axon, the point along the length of axon that had an average numerical value of the axonal diameter was selected.

Because the diameters of myelinated axons and myelin sheaths were noted to vary along the longitudinal axis in both the control and the $Has2^{CKO}$, we also devised an approach which complemented the linear measurements by evaluating cross-sectional areas/unit axonal length. These measures were less susceptible to variability along the axon. Two measurements of areas along 1 µm of axon length were made: (1) axoplasmic area and (2) myelin area, including the area of separation between myelin and axon. A quantity analogous to g-ratio, termed ga-ratio, was then calculated as a ratio of the axoplasmic area to the combined axoplasmic plus myelin area.

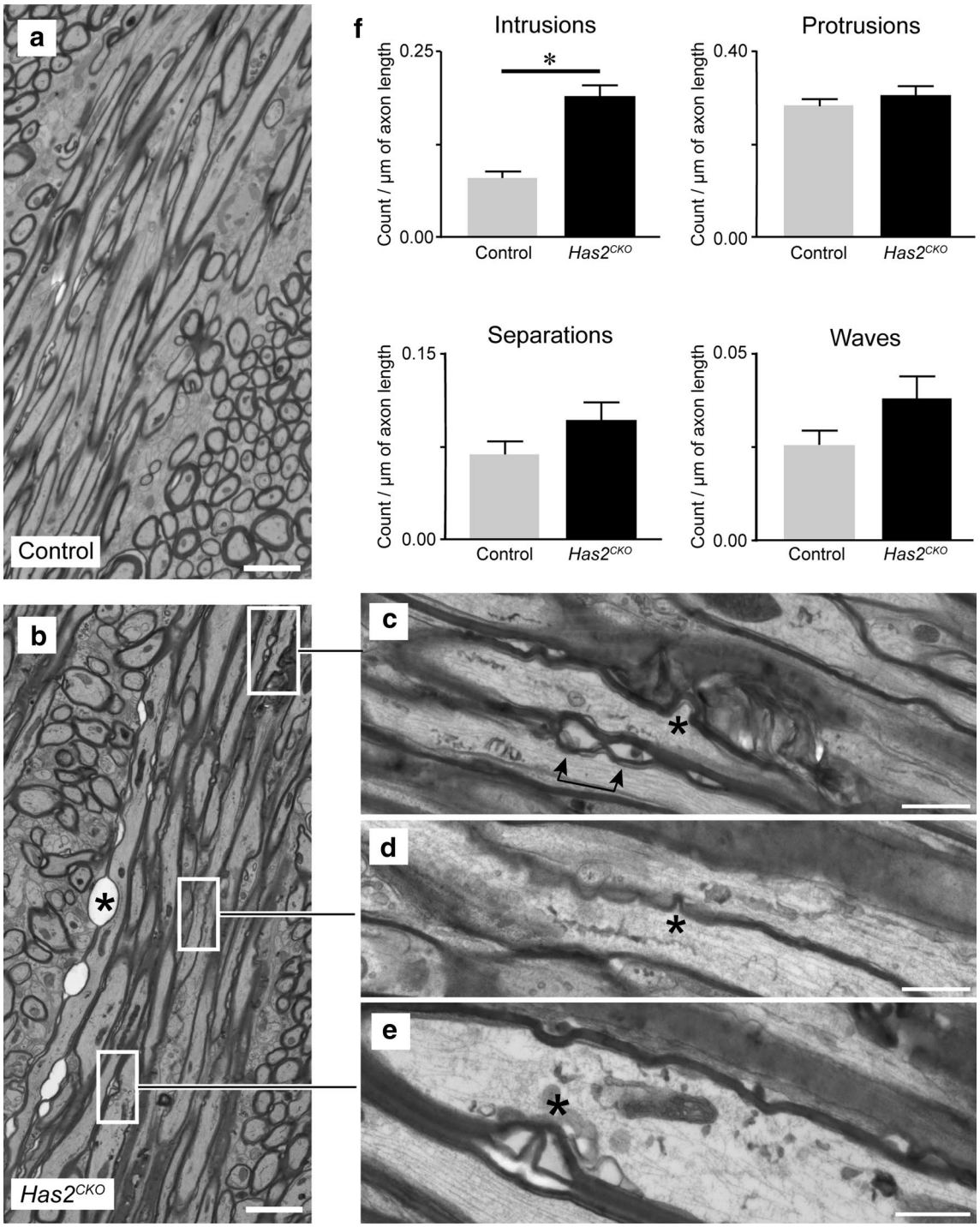

Fig. 1 Quantitative analysis of myelin sheaths in corpus callosum at ultrastructural level. **a**, **b**. Representative micrographs of corpus callosum of a control mouse and a *Has2*^{CKO} mouse at a magnification of 7500×. Scale bar is 2 µm. One type of ultrastructural abnormality, separation (asterisk), is shown in panel (**b**). **c**–**e** Additional abnormalities: protrusions (asterisks, **c**, **d**), wave (dual arrow, **c**), and intrusion (asterisk, **e**) are shown at higher magnification of 30,000×(**c**) and 40,000×(**d**, **e**). Scale bars are 600 nm (**c**) and 500 nm (**d**, **e**). Panel **f** summarizes quantitative analysis of myelin sheaths. Number of events per 1 µm of axon length (mean ± SEM) are plotted. Asterisk denotes statistical significance

Brain Slices Preparation for Diffusion Measurements using Real-Time Iontophoretic Method

For diffusion experiments, five control mice (C57BL6 or *Has2*$^{flox/flox}$; 4.5–8.5 months old, all female) and five *Has2*^{CKO} mice (4.5–8.5 months old, all female) were anesthetized with sodium pentobarbital (50 mg/kg i.p.) and decapitated. During each dissection, the mouse brain was removed from the skull and cooled with ice-cold artificial cerebrospinal fluid (ACSF). Coronal slices 400 µm thick containing the CC with the prevailing direction of fibers running in the plane of a slice were prepared using a microtome with vibrating blade (Leica VT 1000 S; Leica Microsystems, Wetzlar, Germany) as described previously [29]. The slices were submerged in the ACSF in a recovery chamber at room temperature for at least one hour after dissection. The composition of the ACSF was (in mM): NaCl 124, KCl 5, $NaHCO_3$ 26, NaH_2PO_4 1.25, D-glucose 10, $MgCl_2$ 1.3, $CaCl_2$ 1.5. The ACSF was gassed with a 95% O_2 / 5% CO_2 mixture to buffer pH at 7.4. The osmolality of the ACSF, determined with a freezing point-depression osmometer (Osmette A, model no. 5002; Precision Systems Inc., Natick, MA, USA), was 298–305 mosmol/kg. The ACSF used for slice incubation and superfusion contained 0.5 mM of tetramethylammonium (TMA)-chloride. TMA was added to the ACSF to provide a calibration standard.

Real-Time Iontophoretic Method

The Real-Time Iontophoretic (RTI) method [22, 23] with TMA was employed to determine the effective diffusion coefficient D^*, diffusion permeability θ, and the ECS volume fraction α in the CC. TMA was iontophoretically released from a glass microelectrode and detected by an ion-selective microelectrode (ISM) sensing TMA that was positioned approximately 60–100 µm away from the source. RTI measurements were performed along three orthogonal axes positioned along the axons (x-axis) and perpendicularly to them (y-axis and z-axis).

Microelectrodes for iontophoretic release and TMA-ISMs were prepared from double-barreled theta capillary glass (TG200-4; Harvard Apparatus, Holliston, MA, USA), as described previously [30, 31]. Both barrels of the iontophoretic microelectrode were filled with 150 mM TMA-chloride. The ion-detecting barrel of the TMA-ISM was back-filled with 150 mM TMA-chloride and used a short column of tetraphenylborate-based ion exchanger (Corning exchanger 477317, currently available as IE 190 from WPI, Sarasota, FL, USA) at the tip. The DC potential-detecting reference barrel was filled with 150 mM NaCl. Each TMA-ISM was calibrated in a set of standard solutions (0.5, 1, 2, 4, and 8 mM TMA in 150 mM NaCl) before and after each experiment. The calibration voltages were fitted to the Nikolsky equation to obtain the slope and the interference of each TMA-ISM, which were then used for voltage-to-concentration conversion [30].

For each RTI measurement, a specimen (a brain slice or dilute agarose gel in a cup) was placed in a submersion recording chamber (Warner model RC-27L; Harvard Apparatus) and superfused with ACSF flowing at a rate of 2 mL/min. Both the ACSF and the dilute agarose gel (0.3% (w/v) in 150 mM NaCl; NuSieve GTG Agarose, cat# 50081; Lonza, Rockland, ME, USA) contained 0.5 mM TMA-chloride. The temperature of ACSF flowing through the recording chamber was maintained at 33 ± 1 °C by a dual automatic temperature controller (Warner model TC-344B; Harvard Apparatus) operating an in-line heater (Warner model SH-27A; Harvard Apparatus) and a recording chamber heater. The recording chamber was located on a fixed Burleigh Gibraltar platform with an x–y stage (EXFO Photonic Solution, Mississauga, ON, Canada) for a compound microscope (BX51WI; Olympus America, Melville, NY, USA). A CCD camera (OLY 150; Olympus America) attached to the compound microscope was used to visualize the specimen and the microelectrodes held by two independent robotic manipulators (MP285; Sutter Instruments, Novato, CA, USA).

During the RTI measurements, a continuous positive bias current of 20 nA was applied through the iontophoretic microelectrode from a constant-current, high-impedance source (model Axoprobe-A1 Amplifier; Axon Instruments Molecular Devices, Sunnyvale, CA, USA) to maintain a steady transport number (n_t) at all times during the experiment [22, 23]. To obtain a diffusion curve, the current was increased to 40–80 nA for 50 s. The TMA sensing ISM was connected to a dual channel microelectrode preamplifier (model IX2-700; Dagan Corporation, Minneapolis, MN, USA) to amplify the TMA signal obtained by continuously subtracting the DC potential recorded at the reference barrel from that of the ion-detecting barrel, and the DC potential. The TMA and DC signals were further amplified and low-pass filtered (2 Hz) using a signal conditioner (model CyberAmp 320; Axon Instruments Molecular Devices, Union City, CA), then digitized with an analog-to-digital converter (model PCI-MIO-16E-4; National Instruments, Austin, TX, USA) and recorded using the WANDA program [32] written in MATLAB language (MathWorks, Natick, MA, USA).

Acquired diffusion curves were fitted with an appropriate solution of the diffusion equation [22, 24] using a program written in MATLAB language [32]. Diffusion measurements in the dilute agarose gel provided the free diffusion coefficient D_{free} of TMA and the transport number n_t of the iontophoretic microelectrode. Records obtained in the brain slices along three perpendicular axes yielded the effective diffusion coefficient D^* for TMA, the ECS volume fraction α, and the nonspecific clearance k' (s^{-1}) for

each axis [24, 25, 33]. The corresponding diffusion permeabilities were calculated as $\theta_x = D^*_x/D_{\text{free}}$, $\theta_y = D^*_y/D_{\text{free}}$ and $\theta_z = D^*_z/D_{\text{free}}$. The diffusion anisotropy ratio (DAR) was calculated as $DAR = D^*_{along}/D^*_{across}$, where D^*_{along} was measured along the fibers ($D^*_{along} = D^*_x$) while D^*_{across} was averaged from the two measurements across the fibers [$D^*_{across} = (D^*_y + D^*_z)/2$]. ECS volume fraction was calculated as $\alpha = 1/3\ [\alpha_x \times \theta_x / (\theta_y \times \theta_z)^{1/2} + \alpha_y \times \theta_y / (\theta_x \times \theta_z)^{1/2} + \alpha_z \times \theta_z / (\theta_x \times \theta_y)^{1/2}]$ as described previously [24, 33]. After measurements in brain, recordings were taken once more in the dilute agarose gel to verify that n_t remained constant throughout the experiment.

Magnetic Resonance

All data were acquired on a 7.0 T Agilent (Santa Clara, CA, USA) spectrometer with a 40 cm magnet bore, 120 mm gradient coil, maximum gradient strength of 600 mT/m and minimum gradient rise time of 200 µs. The system was equipped with customized shim coils of up to third order. A rapid (Rimpar, Germany) volume transmit coil (72 mm ID) accompanied by a two-channel receive surface coil array were used for radio-frequency transmission and reception, respectively.

For magnetic resonance experiments, four control mice (C57BL6 or $Has2^{flox/flox}$; 6.5–8.5 months old, all female) and five $Has2^{CKO}$ mice (6.5–8.5 months old, all female) were anesthetized using an isoflurane vaporizer set to 3% for induction, reduced to 2% during initial scanner adjustment, and set to 1.5% afterwards. An animal monitoring unit (model 1025; SA Instruments, Stony Brook, NY, USA) was used to record respiration rhythm and rectal temperature. Respiration was measured with a pressure transducer placed under the abdomen just below the rib cage. Body temperature was maintained using forced warm air, controlled by a feedback circuit between the heater and the detecting thermistor. After induction, the animals were placed in a holder and their head movement was restrained with a bite bar and a pair of ear bars. Oxygen was used as the anesthetic carrier gas delivered at a low flow rate of less than 0.5 L/min to a cone positioned before the bite bar where the delivered gas was mixed with air and directed over the nose. All animals were maintained at 37.0 ± 0.2 °C.

Diffusion-Weighted Magnetic Resonance Imaging

Magnetic Resonance Imaging (MRI) can be made sensitive to diffusion. This is achieved by application of paired gradients which make the signal dependent on probabilities that water molecules are displaced by a certain distance during a preset diffusion time. In the case of perfectly Gaussian diffusion, it is sufficient to perform a single measurement along any given direction. Diffusion Tensor Imaging [34, 35] acquires the signal for a single combination of the diffusion time (τ) and the strength of diffusion encoding b (usually referred to as the b-value) but does so repeatedly along several different directions. In CC, the predominant fiber direction is already known, which makes the acquisition time available for further exploration using variable diffusion gradient strengths and diffusion times [36]. In particular, we obtained the Diffusion-Weighted MRI (DW-MRI) signal along and across the fibers as a function of the diffusion time τ and the diffusion gradient encoding strength b because the calculated Apparent Diffusion Coefficient (ADC) can also depend on these variables.

The advantage of DW-MRI is that it assumes the tissue to be homogeneous only within the volume of each imaged voxel, and that it can access much shorter and variable diffusion times and thus smaller spatial features of the CC microenvironment than the RTI diffusion method. Diffusion times can be reduced to several ms, corresponding to root mean square distances of several µm. However, this advantage comes at the considerable price of mixing the intracellular and the extracellular signals [37]. We used diffusion times ranging from 5 to 21 ms and the b values ranging from 475 s/mm^2 to 1900 s/mm^2. However, not all combinations are technically feasible because shorter diffusion times limit the maximum duration of the gradients encoding the diffusion. A total of eight combinations of the diffusion times, the diffusion encoding strengths, and the spatial directions (along or across the axons) were obtained using the spin-echo based diffusion encoded preparation followed by an Echo Planar imaging module [38]. For each combination, eight contiguous slices 500 µm thick were imaged repeatedly eight times with an in-slice resolution of 156 × 156 µm^2. Each diffusion-weighted acquisition was accompanied by a normalizing acquisition with zero b-value and was motion-corrected before averaging the eight repetitions. An additional anatomical scan (described later) with identical location and resolution facilitated selection of a 3D region of interest placed in the CC. This anisotropic region was treated as homogeneous in the subsequent processing. The ADC along and across the axons and the Diffusion Anisotropy Ratios (DAR) defined as a ratio of ADCs along and across the axons were also expressed as percentages of average values obtained from the control mice.

Proton Magnetic Resonance Spectroscopy

Proton Magnetic Resonance Spectroscopy (MRS) is a non-invasive method used to measure the concentrations of brain metabolites. In this study, we used MRS to measure the concentration of N-acetylaspartate (NAA), choline (Cho), creatine (Cr), and glutamate (Glu). The acquisition was a short echo time Point Resolved Spectroscopy (PRESS) [39] sequence with the following parameters: repetition time 4 s,

echo time 7.5 ms, number of averages 512 (34 min acquisition), number of points 2048, and bandwidth of acquisition 5 kHz. The shim settings for the selected voxel of interest (VOI) were automatically adjusted using FASTMAP, Automatic Shimming Technique by Mapping Along Projections [40]. Water suppression was achieved by using variable power radio-frequency pulses with optimized relaxation delays [41]. Outer volume suppression was also used. The voxel of interest size was 9 µl ($1.2\times1.8\times4.2$ mm^3) placed in the center of the CC and adjusted to minimize partial volume effects. All resulting spectral data were processed using the LCModel software developed by Provencher [42]. This software calculates the best fit to the acquired data of a linear combination of model spectra acquired from in vitro solutions. The model spectra consist of all the metabolites of interest. This basis set for the fitting takes into account the field strength, the sequence, and the echo time used. An unsuppressed water signal was also acquired to facilitate normalization. This has several advantages in that it is straightforward to implement, the water suppression option is simply turned off, and it also eliminates several sources of error such as voxel size and relaxation effects. The method assumes that water concentrations with respect to a unit volume of gray or white matter are known and constant [43]. The unsuppressed water signal is also used for eddy current compensation.

Magnetic Resonance Anatomical Imaging

In vivo anatomical scans aided localization of a region of interest in DW-MRI and voxel of interest (VOI) in MRS. Coronal scans were used for DW-MRI and sagittal scans were used for MRS on the same animals. The acquisition sequence was a fast spin echo with the following parameters: repetition time of 4 s, effective echo time of 38.7 ms, echo train length of 8, field of view 20 mm with 156 µm in plane resolution, 8 slices 0.5 mm thick. The total acquisition time was 264 s.

Statistics

Statistical analysis of electron microscopy data was performed with Statistical software GraphPad Prism version 7.0b (GraphPad Software, San Diego, CA, USA). Normality of EM data was determined with D'Agostino-Pearson normality test. The non-parametric statistical test, Mann-Whitney test, was used to test significance of differences between control and *Has2*^{CKO} for all the parameters of axons and myelin sheaths described above. EM data are presented as mean ± SEM, n = number of axons.

Statistical analysis of the RTI data was performed with SigmaStat (Systat Software Inc., San Jose, CA, USA). All RTI data sets were first tested for normality and equal variance in order to determine whether to use a parametric or non-parametric versions of t-test and ANOVA with post hoc test for pairwise multiple comparison procedure. In every slice, 2–4 records were taken along each of the three recording axes and the ECS parameters were averaged for each axis. Since only one slice from an animal was used, each animal provided one value of D^*_x, D^*_y, D^*_z, α and k'. Data are presented as mean ± SEM, n = number of slices, N = number of animals.

Statistical analysis of the MRI data was performed with SigmaStat (Systat Software Inc.). All data sets were first tested for normality and equal variance to determine whether to use a parametric or non-parametric version of t-test and ANOVA with post hoc test for pairwise multiple comparison procedure. Data are presented as mean ± SEM, N = number of animals.

Results

Has2^{CKO} Brains Exhibit Ultrastructural Abnormalities in Myelin Sheaths, Have Smaller Axonal Diameters and Smaller G-Ratios than Control Brains

In the first set of experiments, we evaluated the impact of HA deficiency in the CC on myelinated axons at the ultrastructural level using electron microscopy. We used $n = 252$ axons for control mice and $n = 197$ axons for *Has2*^{CKO} mice. Representative micrographs of myelinated axons from the CC in control and *Has2*^{CKO} mice are shown in Fig. 1a and b, respectively. Magnified micrographs of Fig. 1b show examples of abnormalities in myelin sheaths, such as protrusions (Fig. 1c, d), intrusions (Fig. 1e), and waves (Fig. 1c). Figure 1b also demonstrates separation, another abnormality in myelin sheaths. Significantly greater occurrence of intrusions was found in *Has2*^{CKO} brains (Mann-Whitney test; Fig. 1f, Table 1). The number of protrusions, waves and separations were higher in *Has2*^{CKO} brains but not significantly (Fig. 1f, Table 1).

Next, we measured axon diameters, myelin sheath thickness, and calculated the ratio of axonal diameter to myelinated fiber diameter, i.e. the g-ratio [28], in both groups. The same axons were used as in the analysis of myelin ultrastructure. Axon diameters (without myelin sheaths) were significantly smaller in *Has2*^{CKO} mice while the myelin sheath thickness was not significantly different (Mann-Whitney test; Table 1). The g-ratio of *Has2*^{CKO} was significantly reduced (Mann-Whitney test; Table 1).

Additional measurements relevant to assessing myelin ultrastructure revealed that axon diameter and myelin thickness varied along the lengths of axons. The cross-sectional areas per axonal length approach described in the Materials and Methods was found to be less susceptible to variability

Table 1 Quantification of ultrastructural parameters of myelinated axons in corpus callosum of control and $Has2^{CKO}$ mice

Parameter	Control	$Has2^{CKO}$	*p* value
Intrusions/1 µm of axon length	0.08 ± 0.01	0.18 ± 0.01	0.0001*
Protrusions/1 µm of axon length	0.28 ± 0.01	0.29 ± 0.02	0.659
Waves/1 µm of axon length	0.025 ± 0.004	0.037 ± 0.006	0.263
Separations/1 µm of axon length	0.07 ± 0.01	0.09 ± 0.01	0.195
Axon diameter without myelin sheath (µm)	0.433 ± 0.007	0.414 ± 0.009	0.02*
Myelin sheaths thickness (µm)	0.095 ± 0.002	0.105 ± 0.003	0.179
G-ratio	0.691 ± 0.004	0.664 ± 0.006	0.0003*
Axoplasmic area (μm^2)/1 µm of axon length	0.363 ± 0.006	0.336 ± 0.007	0.0006*
Myelin area (μm^2)/1 µm of axon length	0.241 ± 0.004	0.255 ± 0.007	0.661
Ga-ratio = axoplasmic area (μm^2)/(axoplasmic area + myelin area) (μm^2)	0.597 ± 0.005	0.573 ± 0.006	0.0004*

Values represent mean ± SEM

*Indicates statistical significance at $p < 0.05$

along the axon. The same axonal segments were used as in the analysis of myelin ultrastructure. The results agree in all cases with the corresponding linear measures: the myelin area/axonal length did not differ significantly between the two groups but both the axoplasmic area/axonal length and the ga-ratio were significantly lower in the $Has2^{CKO}$ mice (Mann–Whitney test; Table 1).

Has2^{CKO} Brains Exhibit Greater Extracellular Hindrance to Diffusion and Expanded ECS Volume

In the second set of experiments, we evaluated the impact of HA deficiency in the CC on the structure of ECS. To this end, we employed the RTI method which quantifies the hindrance of extracellular microenvironment to diffusion of a small extracellular probe tetramethylammonium (TMA, 74 MW) as well as the volume occupied by ECS. In an anisotropic white matter tract, diffusion is facilitated in the direction along the axons. The effective diffusion coefficient D^* then becomes a tensor quantity with one principal axis along the direction of the fibers and the remaining two axes in a plane perpendicular to the fibers. It is therefore advantageous to place the RTI microelectrodes accordingly. In each acute brain slice, RTI measurements in the CC were obtained along the axons (*x*-axis) and in two directions perpendicularly to them (*y*-axis and *z*-axis) (Fig. 2a). Diffusion experiments were performed in $n = 5$ slices ($N = 5$ animals) for each group. Figure 2b shows representative diffusion curves (i.e., the concentrations of TMA at the detector as a function of time) in the control and the $Has2^{CKO}$ mice with fitted theoretical curves superimposed. The fitting procedure yielded effective diffusion coefficient D^* for each axis, ECS volume fraction α and non-specific clearance k'. From these measurements, we followed the procedure described in the Materials and Methods to determine effective diffusion tensor components D^*_{along} and D^*_{across} along and across the axons, the corresponding diffusion permeabilities, and also the diffusion anisotropy ratio *DAR* that characterizes the degree of diffusional anisotropy in brain regions containing bundles of axons.

First, we compared the values of D^* within each group to determine whether extracellular diffusion of TMA in the CC was anisotropic, i.e., different between different axes. In both groups, TMA diffused more readily in the direction along the axons than across them ($p < 0.001$, t-test). The values of D^*, θ and *DAR* are reported in Table 2.

Next, we compared values of D^*_{along}, D^*_{across}, *DAR*, α and k' between the two groups. For D^*, we used two-way ANOVA where "genotype" and "axis" were the factors. There was a statistically significant difference indicating that the diffusion was more hindered in the $Has2^{CKO}$ than in the control group (Table 2). ECS volume fraction α was much larger in the $Has2^{CKO}$ than in the control group (t-test; Table 2). *DAR* was smaller in the $Has2^{CKO}$ than in the controls (t-test; Table 2). There was no significant difference in non-specific clearance (t-test; Table 2).

In summary, the RTI measurements indicate that ECS structure is significantly altered in the CC deficient in HA: in $Has2^{CKO}$, extracellular diffusion is more hindered, even though the ECS volume expands by more than 65%.

In Vivo Diffusional Anisotropy is Reduced in *Has2*^{CKO} and the Amount of Freely Moving Water is Increased

In the third set of experiments, we utilized non-invasive in vivo imaging techniques to determine the impact of HA deficiency on water diffusion and on the magnetic resonance spectrum of major brain neurotransmitters and metabolites in the CC. We employed Diffusion-Weighted Magnetic Resonance Imaging (DW-MRI) and Proton Magnetic Resonance Spectroscopy (MRS) in control and $Has2^{CKO}$ mice in vivo.

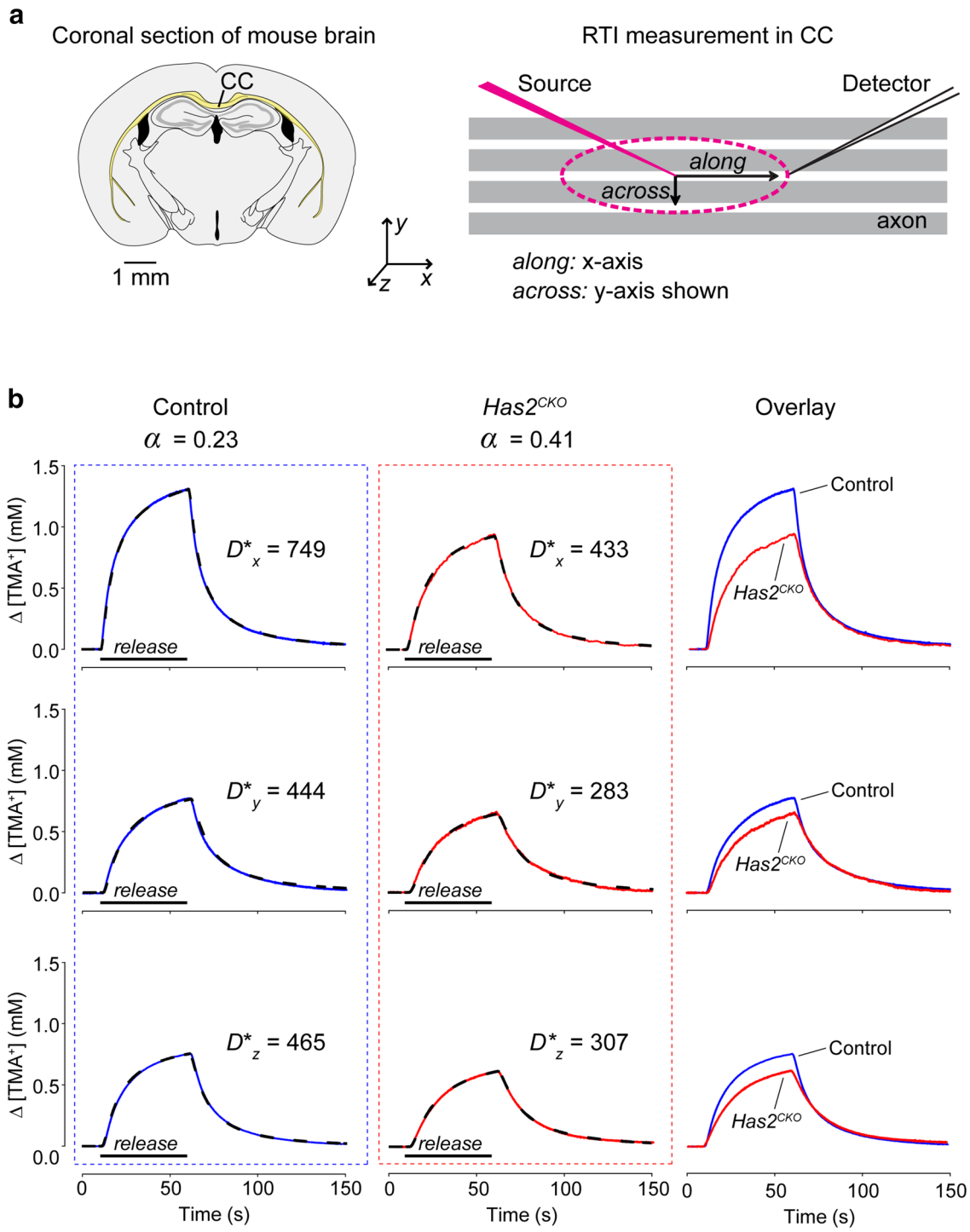

Fig. 2 Extracellular diffusion in corpus callosum measured with RTI. **a** Left panel: cartoon of a coronal section of mouse brain (*CC* corpus callosum). Right panel: schematic of RTI measurement shows placement of the source (iontophoretic microelectrode) and the detector (an ISM sensitive to TMA) with respect to the axons in CC. **b** Representative examples of TMA diffusion records obtained in acute brain slices from a control mouse and a *Has2*^{CKO} mouse. The theoretical curves (dashed lines) are superimposed on the TMA diffusion curves (solid lines). A horizontal bar below each diffusion record marks the duration of TMA iontophoretic release. Values of D^* ($\mu m^2/s$) are at 34 °C. Diffusion permeabilities were $\theta_x = 0.607$, $\theta_y = 0.361$, $\theta_z = 0.375$ in a control mouse and $\theta_x = 0.355$, $\theta_y = 0.233$, $\theta_z = 0.252$ in a *Has2*^{CKO} mouse. Non-specific clearance *k'* was 0.0078 s^{-1} in a control mouse and 0.0097 s^{-1} in a *Has2*^{CKO} mouse. For all records, $r = 100$ µm and $n_t = 0.393$. The overlay column enables a direct comparison of the diffusion curves obtained in a control mouse and a *Has2*^{CKO} mouse

Table 2 ECS structural parameters determined with RTI in corpus callosum of control and *Has2*^{CKO} mice

Parameter	Control	*Has2*^{CKO}	Relative change in *Has2*^{CKO} (control = 100%)	*p* value
D^*_{along} (μm^2/s)	664 ± 27	433 ± 7	65. 2	0.001*
θ_{along}	0.535	0.349		
D^*_{across} (μm^2/s)	406 ± 26	313 ± 17	77.1	
θ_{across}	0.327	0.252		
DAR	1.64 ± 0.05	1.40 ± 0.06	85.4	0.011*
α	0.228 ± 0.011	0.381 ± 0.015	167.1	0.001*
k' (s^{-1})	0.010 ± 0.002	0.010 ± 0.002	100	0.937

D^* of TMA was measured at 34 °C; $D^*_{along} = D^*_x$; $D^*_{across} = (D^*_y + D^*_z)/2$

D_{free} of TMA at 34 °C is 1240 μm^2/s

Diffusion permeability $\theta = D^*/D_{free}$, tortuosity $\lambda = 1/\sqrt{\theta}$

Values represent mean ± SEM

*Indicates statistical significance at $p < 0.05$

Using DW-MRI, we measured apparent diffusion coefficient (*ADC*) of water along the axons and across the axons for five diffusion encoding strengths (*b*) and five diffusion times (τ) in control mice ($N = 3$) and in *Has2*^{CKO} mice ($N = 5$) (Fig. 3). In contrast to RTI, DW-MRI reflects a mixture of intracellular and extracellular diffusion. Even so, reduction of water diffusion along the axons and reduction of anisotropy was found in the CC of *Has2*^{CKO} mice. These reductions are more pronounced and statistically significant at longer diffusion times (*ADC*: ANOVA, *DAR*: t-test; Table 3).

Figure 4a shows typical examples of proton spectra from a control mouse and a *Has2*^{CKO} mouse, acquired in the CC. The VOI is highlighted on the anatomical reference scan used for voxel placement (Fig. 4b). The water-referenced concentrations of total N-acetylaspartate (tNAA), total of all creatine containing compounds (tCr), total of all choline containing compounds (tCho) and total glutamate and glutamine (tGlu) from the control mice ($N = 4$) and the *Has2*^{CKO} mice ($N = 4$) are reported in Table 4. The *Has2*^{CKO} appears to have reduced concentrations of all of these compounds, two of them significantly (t-test, Table 4). However, had the concentrations been referenced to creatine, there would be no significant differences between the groups. It is therefore likely that the real change occurred instead in the amount of water visible to the MRS, i.e., by releasing molecules from the pool of fast-relaxing water inside the myelin sheaths. This would increase the amount of water with slower transverse relaxation, increase the total water signal used as a normalization factor, and thus lead to an apparent reduction of all other compounds.

Discussion

We applied a multi-scale approach encompassing electron microscopy, extracellular diffusion analysis, and in vivo magnetic resonance imaging and spectroscopy to study how the deficiency in HA, which is a major component of brain ECM, impacts the structure and function of white matter. The *Has2*^{CKO} mice served as a model of a significant HA loss in the CC, as previously reported by Arranz et al. [17]. In *Has2*^{CKO} mice, we have found (1) at the ultrastructural level, abnormalities in myelin sheaths and reduction of axonal diameter (2) at the microscopic level, grossly enlarged and geometrically more complex ECS, and (3) at the macroscopic level in vivo, diminished apparent diffusion rates along the axons and increased amount of freely moving water. These findings have implications for saltatory propagation of axon potentials and for transport of solutes and signaling molecules in the white matter ECS. They point to the importance of HA for the integrity of myelin sheaths.

A number of previous studies employed electron microscopy to study the ultrastructure of CC in mice. Sturrock [44] studied the ultrastructure of CC in mice between birth and 8 months of age and reported that the mean diameter of myelinated axons was 0.46 μm. Lehman and co-workers [45] studied corpus callosum in 2 months old mice and reported that 73% of myelinated axons were of a small to medium caliber with an average axon diameter in the range from 0.414 to 0.641 μm and average myelin thickness in the range from 0.093 to 0.109 μm, yielding g-ratios from 0.82 to 0.855. The remaining 27% of myelinated axons were of a large caliber with the average axon diameter of 1.028 μm and the average myelin thickness of 0.131 μm, yielding the g-ratio of 0.887. Heterogeneity of CC with respect to axonal diameter and greater g-ratio for large caliber axons have also been reported by others [28]. Our estimates of the axonal diameter, the myelin thickness and the g-ratio agrees with the values reported for myelinated axons of small to medium caliber.

Bekku and co-workers [8] studied the ultrastructural organization of myelinated axons in Bral1-deficient mice. Bral1 is an ECM protein that links HA to the lectican family

a

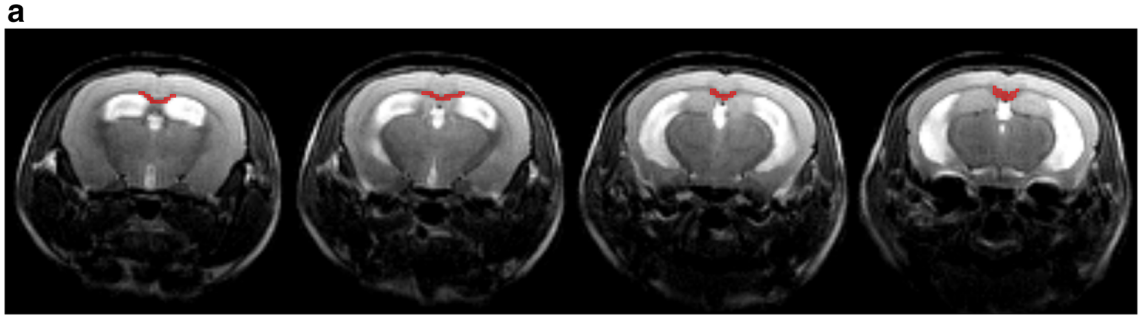

b

Relative change of ADC_{along} in $Has2^{CKO}$

b \ τ	5	9	13	17	21
475	101.5	106.9	103.0	97.2	89.8
831		101.1	94.8	93.3	94.6
1188			94.0	92.6	93.1
1544				92.4	92.3
1900					92.1

Relative change of ADC_{across} in $Has2^{CKO}$

b \ τ	5	9	13	17	21
475	108.5	118.8	112.4	105.4	101.4
831		110.2	108.9	104.1	109.6
1188			106.9	103.6	105.9
1544				101.5	104.5
1900					104.5

c

Relative change of *DAR* in $Has2^{CKO}$

b \ τ	5	9	13	17	21
475	93.5	90.0	91.6	92.3	88.6
831		91.7	87.0	89.6	86.3
1188			87.9	89.4	87.9
1544				91.0	88.3
1900					88.2

Fig. 3 In vivo Diffusion-Weighted MRI in corpus callosum. **a** Four anatomical coronal sections (out of eight acquired) of a $Has2^{CKO}$ brain in vivo are shown. A region of interest (red) inside CC where *ADC* was quantified is marked. **b** Summary of relative changes in *ADC* measured along the axons and across the axons in the CC of $Has2^{CKO}$ mice relative to *ADC* measured along and across the axons in the CC of control mice (set to 100%). *ADC*, apparent diffusion coefficient; τ, diffusion time (ms); *b*, diffusion encoding strength (s/mm^2). **c** Summary of relative changes in *DAR* in the CC of $Has2^{CKO}$ mice relative to *DAR* in the CC of control mice (set to 100%). *DAR*, diffusion anisotropy ratio

Table 3 In vivo DW-MRI in corpus callosum of control and $Has2^{CKO}$ mice at τ = 21 s

Parameter	Control	$Has2^{CKO}$	Relative change in $Has2^{CKO}$ (control = 100%)	*p* value
ADC_{along} (μm^2/s)	821.3 ± 22.4	746.1 ± 21.3	90.8	0.03*
ADC_{across} (μm^2/s)	460.2 ± 13.8	483.9 ± 13.2	105.1	0.141
DAR	1.76 ± 0.03	1.55 ± 0.03	88.1	0.001*

Values represent mean ± SEM

*Indicates statistical significance at $p < 0.05$

chondroitin sulfate proteoglycans and plays an important role in stabilizing ECM at the nodes of Ranvier. Although no quantification was provided, their inspection of the ultrathin transverse sections of an optic nerve revealed no differences in myelin sheath thickness and compaction between the Bral1-deficient mice and the wild-type mice. They concluded that Bral1 is not required for myelin formation and maintenance. In contrast, we found significant changes in the ultrastructure of myelinated axons in HA-deficient CC of $Has2^{CKO}$ mice. The HA deficiency did not significantly change the thickness of myelin but it did have impact on myelin integrity. The most prominent example among the various abnormalities observed in $Has2^{CKO}$ mice was the number of myelin intrusions, which more than doubled in the CC of $Has2^{CKO}$ mice compared with the CC of control mice. Intrusions of myelin sheaths affect the structural

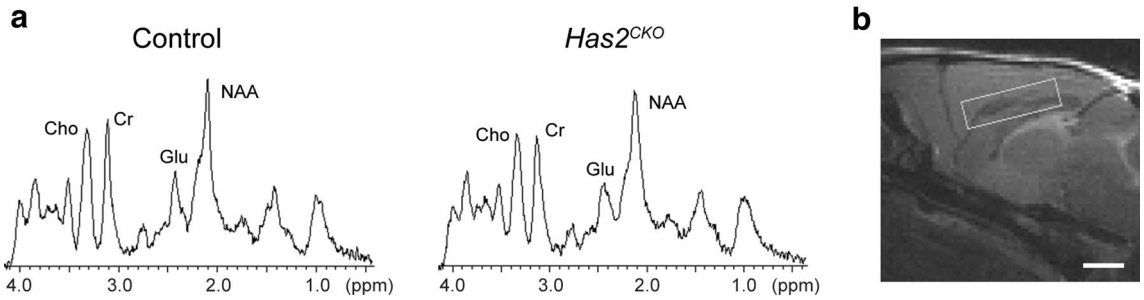

Fig. 4 In vivo proton MRS in corpus callosum. **a** Representative spectra obtained from a control mouse and a *Has2*^{CKO} mouse. The principal resonances of N-acetyaspartate (NAA), choline (Cho), creatine (Cr) and glutamate (Glu) are marked in each spectrum. **b** Voxel of interest (VOI) is highlighted (*white*) on the anatomical reference scan. The scale bar is 2 mm long

Table 4 Water-referenced concentrations of major neurotransmitters and metabolites in corpus callosum of control and *Has2*^{CKO} mice in vivo

Substance	Control	*Has2*^{CKO}	Relative change in *Has2*^{CKO} (Control = 100%)	*p* value
tNAA (mM)	7.70 ± 0.28	6.40 ± 0.69	83.1	0.124
tCr (mM)	6.44 ± 0.38	5.37 ± 0.5	83.4	0.0025*
tCho (mM)	1.64 ± 0.09	1.37 ± 0.11	83.5	0.064
tGlu (mM)	11.12 ± 0.38	8.81 ± 0.71	79.2	0.031*

tNAA = NAA + NAAG, tCr = Cr + PCr, tCho = PCh + GPC, tGlu = Glu + Gln

where *NAA* N-acetylaspartate, *NAAG* N-acetyl aspartylglutamate, *Cr* creatine, *PCr* phosphocreatine, *PCh* phosphocholine, *GPC* glycerophosphocholine, *Glu* glutamate, *Gln* glutamine

Values represent mean ± SEM

*Indicates statistical significance at $p < 0.05$

integrity of myelinated axon fibers; they bend the outer myelin lamellae into the inner lamellae, loosening the myelin compactness and opening void spaces within the myelin sheath. Intrusions also locally compress the axonal membrane, pinching the axonal diameter. Overall, the abnormalities combined to diminish the adherence of myelin lamellae. This could be explained by HA being present inside the myelin sheaths [16] and at the nodes of Ranvier [8, 14, 15]. We propose that HA is the main molecular player responsible for the structural stability of the periaxonal environment, including the myelin lamellae. The HA deficiency also affected axonal morphology. In particular, the axonal diameter was significantly reduced, which was also reflected in the reduced g-ratio.

Our extracellular diffusion results in control mice agree with previous studies in the CC of rats and mice [8, 46] but the RTI measurements in the *Has2*^{CKO} reveal that HA deficiency has much more profound effect on the ECS structure and extracellular diffusion than found in the CC of Bral1 deficient mouse [8]. RTI studies in Bral1-deficient mice described increased diffusion rates along and across the axons, and no change in ECS volume. In white matter, HA stabilizes assembly of densely organized ECM at the nodes of Ranvier [47] and its removal results in a loss of nodal expression for several lecticans and tenascin R [8]. It was proposed that negatively-charged matrix assembly at the nodes of Ranvier sequesters cations that are needed to support saltatory conduction of action potential along myelinated axons, and that disturbed perinodal milieu by removal of Bral1 explains a reduced propagation of action potentials in Bral1-deficient mice [8]. Removal of HA had very different effect on ECS structure and extracellular diffusion than Bral1 knockout, impacting both hindrance to diffusion and ECS volume. HA is a major component of ECS and it is often described as a backbone of extracellular matrix that is anchored in cellular membranes either by remaining attached to its synthesizing enzyme or via interaction with HA receptors, CD44 and RHAMM (Receptor for Hyaluronan Mediated Motility). Other matrix molecules interact with HA either directly or indirectly and HA is a core organization structure of matrix assemblies. Interestingly, knockout of *Has3*, another *Has* subtype expressed primarily in neuronal cells, results in a decrease in the ECS volume and an increase in excitability of CA1 neurons in the stratum pyramidale of hippocampus, while causing little structural change in the strata radiatum and oriens [17]. In contrast, we observed a significant ECS enlargement and disruption of myelin structure in *Has2*^{CKO}. This suggests that HA has distinct functions in white matter and gray matter. Given the striking structural abnormalities of the myelin sheath in *Has2*^{CKO} mice, HA may play a role in the compaction of myelin lamellae, in addition to its role in ECM assembly. Alternatively, the difference in the effect on the ECS volume may be due to the fact that HAS2 and HAS3 synthesize HA of different molecular size.

It would be expected that the voids in myelin increase the proportion of dead spaces inside the white matter ECS, resulting in a reduction of effective diffusion rates as predicted by the diffusion dwell-time mechanism [21]. Dead

spaces transiently trap diffusing molecules and slow down their diffusion through the ECS. Reduced effective diffusion rates were indeed detected by the extracellular diffusion method. The RTI measurements also found much larger total extracellular volume, by more than 65%, in the HA-deficient white matter. However, assuming a uniform reduction of the axonal diameters equal to the average decrease we observed, this reduction alone could be responsible for at most a 15% increase in ECS volume. Only if most of the myelin sheath volume becomes interconnected with the ECS space can we explain the ECS volume increase detected by the RTI method. It therefore seems likely that the myelination abnormalities are not restricted to parts of axonal fibers but instead the entire wrapping becomes loosened and accessible from the ECS. The dwell-time diffusion theory [21] predicts the dead space volume fraction $\alpha_d = \alpha - 3\ \alpha\ \theta/(2+\alpha\ \theta)$, where θ is the diffusion permeability. The much higher diffusional hindrance (that is, much lower θ) in HA-deficient CC can therefore be explained only if almost the entire added ECS volume is in the form of dead spaces. Such dead spaces may be created by invaginations formed by the loosened myelin wrappings. This also means that the myelin sheaths are likely to be connected to the rest of the ECS in only a limited number of places, e.g., at the nodes, because high density of connections would prevent them from playing their dead-space role.

The DW-MRI measurements mostly confirmed the RTI results in vivo. Diffusion rate along the white matter fibers (but not across) was significantly diminished, especially for longer diffusion times. There was no indication that the diffusion became non-Gaussian as the apparent diffusion rates did not vary significantly with the diffusion gradient strength. However, it is important to realize that in contrast to RTI, MRI detects both the extracellular and intracellular water molecules, and that the diffusion times and typical molecular displacements are very different. Even for the longest diffusion time used, the root mean square displacement would not exceed several micrometers in DW-MRI while it is on the order of 100 micrometers in the RTI method. In view of our other results, it is likely that the DW-MRI at shorter diffusion times did not provide enough time for the molecules to fully explore the geometrically complex environment, thus possibly overestimating the diffusion rates in $Has2^{CKO}$ mice [48]. A comparison with Bral1 study [8] leads to the same conclusion as the RTI measurements. The authors found that the diffusion rates increased in the Bral1 KO mice, an effect opposite to that of HA deficiency.

The proton MRS found that the $Has2^{CKO}$ white matter had reduced ratios of concentrations of several major brain metabolites to the concentration of water visible to the MRS. In agreement with our other results, we interpret this finding to mean that water was released from the confinement of myelin sheaths, where it would have very short transverse relaxation time, into the free water pool of the ECS. Because the ECS water pool has much longer transverse relaxation time, the water signal increases [49, 50]. The amounts of detected change in relative metabolite to water concentrations are consistent with the increase of ECS volume measured by the RTI method. In contrast to a recent study where cuprizone was used to demyelinate axons in mice [51, 52], we have not detected any significant changes in substance concentrations referenced to total creatine. This is consistent with our electron microscopy results which did not indicate a significant loss of myelin.

In summary, this work has demonstrated that HA is an important player in the periaxonal environment of white matter. Together with the previous Bral1 study [8], it has begun to unveil the specific roles played by different matrix components.

Acknowledgements This work was supported by National Institutes of Health National Institute of Neurological Disorders and Stroke grant R01 NS047557 to SH and CA, National Institutes of Health National Institute of Neurological Disorders and Stroke grant R01 NS066019 to CA, National Institutes of Health National Institute of General Medical Sciences grant R25 GM097634 to CA, National Institutes of Health National Institute of Aging grant RF1 AG057579 to YY, National Institutes of Health National Eye Institute Core grant EY13079 to the Center for Neural Science, New York University, and National Institutes of Health National Center for Research Resources shared instrumentation grant S10 RR023534 to Nathan S. Kline Institute.

Compliance with Ethical Standards

Ethical Approval All applicable international, national, and/or institutional guidelines for the care and use of animals were followed. All protocols for animal use were in accordance with the National Institute of Health Guidelines and approved by the local Institutional Animal Care and Use Committees at Sanford Burnham Prebys Medical Discovery Institute, State University of New York Downstate, and Nathan S. Kline Institute. This article does not contain any studies with human participants performed by any of the authors.

References

1. Bengtsson SL, Nagy Z, Skare S, Forsman L, Forssberg H, Ullen F (2005) Extensive piano practicing has regionally specific effect on white matter development. Nat Neurosci 8:1148–1150
2. Scholz J, Klein MC, Behrens TEJ, Johansen-Berg H (2009) Training induces changes in white-matter architecture. Nat Neurosci 12:1370–1371
3. Lassmann H, Brück W, Lucchinetti C (2007) The immunopathology of multiple sclerosis: an overview. Brain Pathol 17:210–218
4. Marret S, Vanhulle C, Laquerriere A (2013) Pathophysiology of cerebral palsy. Handb Clin Neurol 111:169–176
5. Armstrong RD, Mierzwa AJ, Marion CM, Sullivan GM (2016) White matter involvement after TBI: clues to axon and myelin repair capacity. Exp Neurol 275:328–333
6. Fields RD (2008) White matter in learning, cognition and psychiatric disorders. Trends Neurosci 31:361–370

7. Filley CM, Fields RD (2016) White matter and cognition: making the connection. J Neurophysiol 116:2093–2104
8. Bekku Y, Vargova L, Goto Y, Vorisek I, Dmytrenko L, Narasaki M, Ohtsuka A, Fassler R, Ninomiya Y, Sykova E, Oohashi T (2010) Bral1: its role in diffusion barrier formation and conduction velocity in the CNS. J Neurosci 30:3113–3123
9. Yamaguchi Y (2000) Lecticans: organizers of the brain extracellular matrix. Cell Mol Life Sci 57:276–289
10. Dityatev A, Seidenbecher CI, Schachner M (2010) Compartmentalization from the outside: the extracellular matrix and functional microdomains in the brain. Trends Neurosci 33:503–512
11. Smith PD, Coulson-Thomas VJ, Foscarin S, Kwok JC, Fawcett JW (2015) "GAG-ing with neurons": the role of glycosaminoglycans patterning in the central nervous system. Exp Neurol 274:100–114
12. Toole BP (2004) Hyaluronan: from extracellular glue to pericellular cue. Nat Rev Cancer 4:528–539
13. Toole BP (2000) Hyaluronan is not just a goo! J Clin Invest 106:335–336
14. Delpech B, Delpech A, Bruckner G, Girard N, Maingonnat C (1989) Hyaluronan and hyaluronectin in the nervous system. Ciba Found Symp 143:208–220; (discussion 21–32, 81–85).
15. Girard N, Courel MN, Delpech A, Bruckner G, Delpech B (1992) Staining of hyaluronan in rat cerebellum with a hyaluronectin-antihyaluronectin immune complex. Histochem J 24:21–24
16. Eggli PS, Lucocq Ott P, Graber W, van der Zypen E (1992) Ultrastructural localization of hyaluronan in myelin sheaths of the rat central and rat and human peripheral nervous systems using hyaluronan-binding protein-gold and link protein-gold. Neuroscience 48:137–744
17. Arranz A, Perkins KL, Irie F, Lewis DP, Hrabe J, Xiao F, Itano N, Kimata K, Hrabetova S, Yamaguchi Y (2014) Hyaluronan deficiency due to *Has3* knock-out causes altered neuronal activity and seizures via reduction in brain extracellular space. J Neurosci 34:6164–6176
18. Sykova E, Nicholson C (2008) Diffusion in brain extracellular space. Physiol Rev 88:1277–1340
19. Sykova E, Vorisek I, Mazel T, Antonova T, Schachner M (2005) Reduced extracellular space in the brain of tenascin-R- and HNK-1-sulphotransferase deficient mice. Eur J Neurosci 22:1873–1880
20. Nicholson C (2001) Diffusion and related transport mechanisms in brain tissue. Rep Prog Phys 64:815–884
21. Hrabe J, Hrabetova S, Segeth K (2004) A model of effective diffusion and tortuosity in the extracellular space of the brain. Biophys J 87:1606–1617
22. Nicholson C, Phillips JM (1981) Ion diffusion modified by tortuosity and volume fraction in the extracellular microenvironment of the rat cerebellum. J Physiol 321:225–257
23. Odackal J, Colbourn R, Odackal NJ, Tao L, Nicholson C, Hrabetova S (2017) Real-time iontophoresis with tetramethylammonium to quantify volume fraction and tortuosity of brain extracellular space. J Vis Exp 125:e55755
24. Rice ME, Okada YC, Nicholson C (1993) Anisotropic and heterogeneous diffusion in the turtle cerebellum: implications for volume transmission. J Neurophysiol 70:2035–2044
25. Vorisek I, Sykova E (1997) Evolution of anisotropic diffusion in the developing rat corpus callosum. J Neurophysiol 78:912–919
26. Aoki C, Rodrigues S, Kurose H (2000) Use of electron microscopy in the detection of adrenergic receptors. In: Machida C (ed) Methods in molecular biology: adrenergic receptor protocols, Humana, pp. 535–563.
27. Hooshmand MJ, Anderson AJ, Cummings BJ (2014) Improved pre-embedded immuno-electron microscopy procedures to preserve myelin integrity in mammalian central nervous tissue. In: Mendex-Vilas A (eds) Microscopy: advances in scientific research and education. pp. 59–65.
28. West KL, Kelm ND, Carson RP, Does MD (2015) Quantitative analysis of mouse corpus callosum from electron microscopy images. Data Brief 5:124–128
29. Xiao F, Hrabetova S (2009) Enlarged extracellular space of aquaporin-4-deficient mice does not enhance diffusion of Alexa Fluor 488 or dextran polymers. Neuroscience 161:39–45
30. Nicholson C (1993) Ion-selective microelectrodes and diffusion measurements as tools to explore the brain cell microenvironment. J Neurosci Methods 48:199–213
31. Hrabetova S (2005) Extracellular diffusion is fast and isotropic in the stratum radiatum of hippocampal CA1 region in rat brain slices. Hippocampus 15:441–450
32. Hrabetova S, Nicholson C (2007) Biophysical properties of brain extracellular space explored with ion-selective microelectrodes, integrative optical imaging and related techniques. In: Michael AC, Borland LM (eds) Electrochemical methods for neuroscience. CRC, Florida, pp 167–204
33. Sykova E, Mazel T, Hasenohrl RU, Harvey AR, Simonova Z, Mulders WHAM, Huston JP (2002) Learning deficits in aged rats related to decrease in extracellular volume and loss of diffusion anisotropy in hippocampus. Hippocampus 12:269–279
34. Basser PJ, Mattiello J, LeBihan D (1994) Estimation of the effective self-diffusion tensor from the NMR spin echo. J Magn Reson B 103:247–254
35. Basser PJ, Pierpaoli C (1996) Microstructral and physiological features of tissues elucidated by quantitative diffusion tensor MRI. J Magn Reson 111:209–219
36. Callaghan PT (1991) Principles of nuclear magnetic resonance microscopy. Oxford University Press, New York
37. Hrabe J, Kaur G, Guilfoyle DN (2007) Principles and limitations of NMR diffusion measurements. J Med Phys 32:34–42
38. Mansfied P (1977) Multi-planar image formation using NMR spin echoes. J Phys C 10:L55–L58
39. Bottomley PA (1987) Spatial localization in NMR spectroscopy in vivo. Ann NY Acad Sci USA 508:333–348
40. Gruetter R (1993) Automatic, localized in vivo adjustment of all first- and second-order shim coils. Magn Reson Med 29:804–811
41. Tkac I, Starcuk Z, Choi IY, Gruetter R (1999) In vivo ^{1}H NMR spectroscopy of rat brain at 1 ms echo time. Magn Reson Med 41:649–656
42. Provencher SW (1993) Estimation of metabolite concentrations from localized in vivo proton NMR spectra. Magn Reson Med 30:672–679
43. Ernst T, Kreis R, Ross BD (1993) Absolute quantitation of water and metabolites in the human brain. I. Compartments and water. J Magn Reson B 102:1–8
44. Sturrock RR (1980) Myelination of the mouse corpus callosum. Neuropathol Appl Neurobiol 6:415–420
45. Lehman DM, Hale DE, Cody JT, Harrison JM, Leach RJ (1999) Molecular, morphometric and functional analyses demonstrate that the growth hormone deficient little mouse is not hypomyelinated. Dev Brain Res 116:191–199
46. Sykova E, Mazel T, Simonova Z (1998) Diffusion constrains and neuron-glia interaction during aging. Exp Gerontol 33:837–851
47. Oohashi T, Hirakawa S, Bekku Y, Rauch U, Zimmermann DR, Su WD, Ohtsuka A, Murakami T, Ninomiya Y (2002) Bral1, a brain-specific link protein, colocalizing with the versican V2 isoform at the nodes of Ranvier in developing and adult mouse central nervous systems. Mol Cell Neurosci 19:43–57
48. Xiao F, Hrabe J, Hrabetova S (2015) Anomalous extracellular diffusion in rat cerebellum. Biophys J 108:2384–2395
49. Menon RS, Allen PS (1991) Application of continuous relaxation time distributions to the fitting of data from model systems and excised tissue. Magn Reson Med 20:214–227
50. MacKay AL, Laule C (2016) Magnetic resonance of myelin water: An in vivo marker for myelin. Brain Plast 2:71–91

51. Orije J, Kara F, Guglielmetti C, Praet J, Van der Linden A, Ponsaerts P, Verhoye M (2015) Longitudinal monitoring of metabolic alterations in cuprizone mouse model of multiple sclerosis using 1H-magnetic resonance spectroscopy. Neuroimage 114:128–135
52. Matsushima GK, Morell P (2001) The neurotoxicant, cuprizone, as a model to study demyelination and remyelination in the central nervous system. Brain Pathol 11:107–116